Constructing the equation of state of QCD in a functional QCD based scheme

Yi Lu,[1,†] Fei Gao,[2,*] Baochi Fu,[1,‡] Huichao Song,[1,3,4,§] and Yu-xin Liu[1,3,4,‖]

[1]*Department of Physics and State Key Laboratory of Nuclear Physics and Technology, Peking University, Beijing 100871, China*

[2]*School of Physics, Beijing Institute of Technology, Beijing 100081, China*

[3]*Center for High Energy Physics, Peking University, Beijing 100871, China*

[4]*Collaborative Innovation Center of Quantum Matter, Beijing 100871, China*

(Received 1 November 2023; accepted 16 May 2024; published 21 June 2024)

We construct the equation of state (EOS) of QCD based on the finite chemical potential information from the functional QCD approaches with the results at zero chemical potential being calibrated by lattice QCD simulations. Specifically, the construction is achieved by parametrizing the order parameters from the functional QCD data into the EOS, namely, the dynamical quark mass for the chiral phase transition and the Polyakov loop for the deconfinement phase transition. The obtained EOS is consistent with the up-to-date results of the QCD phase diagram, including a phase transition temperature at zero chemical potential of $T = 155$ MeV, the curvature of the transition line $\kappa = 0.016$, and also a critical end point at $(T, \mu_B) = (118, 600)$ MeV. We also implement the EOS in hydrodynamic simulations to compute the particle yields and ratios and find that our obtained EOS agrees well with the commonly used one based on the combination of lattice QCD simulation and hadron resonance gas model.

DOI: 10.1103/PhysRevD.109.114031

I. INTRODUCTION

One of the main goals of the relativistic heavy-ion collision experiments is to search for the critical end point (CEP) of the QCD matter and to explore the thermodynamic properties of the strong interaction matter at finite temperature and chemical potential [1–6]. To build the bridge between these measurements and the theoretical studies, the key element is the equation of state (EOS) of the QCD matter [7–13], since the EOS plays a crucial role as the input in hydrodynamic simulations for the evolution of the fireballs produced in heavy-ion collisions.

On the theoretical side, the QCD phase diagram has been widely studied via effective models [14–27] and the QCD approaches like lattice QCD simulation [28–30] and functional QCD (fQCD) methods including the Dyson-Schwinger equations (DSEs) [31–38] and functional renormalization group (fRG) approach [39–41]. Among them, the functional QCD methods have delivered a comprehensive investigation on the phase diagram and, especially, on the location of the CEP at large chemical potential. The current computations have given the phase transition line which is consistent with the lattice QCD simulation at small chemical potential. The functional QCD approaches also provided an estimate of the CEP at about $\mu_B \approx 600$ to 650 MeV [36–39]. However, there is still no complete computation for the EOS which matches these up-to-date results for the phase transition line and is accessible for the hydrodynamics simulations. The estimated CEP is not even incorporated in the commonly applied EOS.

In this article, we then take advantage of different theoretical approaches to obtain an improved construction on the EOS. It incorporates the order parameters from the functional QCD results, including a quantitatively reliable phase transition line with the pseudocritical temperature, the curvature at small chemical potential, and the location of the CEP at large chemical potential, together with the assistance of the lattice EOS at zero chemical potential. The constructed EOS is also required to satisfy the constraints from the current results of the thermodynamic quantities. All the elements in the construction are formularized analytically, making the further application of the EOS accessible and convenient. We also incorporate our EOS into hydrodynamic simulations to compute the experimental observables like the particle yields, collective flow, and so on.

The article is organized as follows. In Sec. II, we discuss the order parameters of the QCD phase transitions and their parametrizations from the functional QCD data. In Sec. III,

*Corresponding author: fei.gao@bit.edu.cn
†qwertylou@pku.edu.cn
‡fubaochi@pku.edu.cn
§huichaosong@pku.edu.cn
‖yxliu@pku.edu.cn

we present the framework of constructing the EOS from the obtained order parameters. In Sec. IV, we show the numerical results of EOS in the (μ_B, T) plane and also the Maxwell construction in the first-order phase transition which stablizes the evolution. This then enables us to present the results of particle yields after incorporating with the hydrodynamic simulation. In Sec. V, we summarize the main results and discuss a few things.

II. QCD PHASE STRUCTURE AND THE ORDER PARAMETERS

Over the past few years, the functional QCD approaches, i.e., the DSEs approach [31,35,42,43] and the fRG approach [40,44], has been well developed and applied to the study on the QCD phase structure at finite temperature and baryon chemical potential. At small chemical potential, the two functional approaches have met the lattice QCD results quantitatively, in particular for the QCD chiral phase transition line:

$$\frac{T_c(\mu_B)}{T_c(0)} = 1 - \kappa\left(\frac{\mu_B}{T_c(0)}\right)^2 + \kappa_4\left(\frac{\mu_B}{T_c(0)}\right)^4 + \cdots. \quad (1)$$

For the $(2+1)$-flavor case, the consistent results (central averages) are $T_c(0) = 155$ MeV, $\kappa = 0.016$ [28–30,37,39]. On the other hand, at large chemical potential, the two functional approaches are also converging with each other, including an estimation on the small fourth-order curvature $|\kappa_4| \simeq \mathcal{O}(10^{-4})$ and the location of the CEP at about $\mu_B^{\rm CEP} \approx$ 600 to 650 MeV [37–39,45]. More specifically, Ref. [38] and a series of studies such as Ref. [46] have also demonstrated the emergent hadrons effect on the chiral phase transition, particularly for the pseudo-Goldstone modes. Such an effect is included in the quark gap equation through the hadron resonance channel, which is found to be subleading with only a small effect on the chiral phase transition temperature and the CEP location. This gives then a strong constraint on the order parameter of chiral phase evolution.

There are also some predictions on the deconfinement phase transition from the functional approaches which have shown some connections to the chiral phase transition; see, e.g., Refs. [33,39,47]. In this work, we then focus on the chiral phase transition and the deconfinement phase transition, which characterize mainly the physics processes in the heavy-ion collision experiment with typical temperature $T \gtrsim$ 100 MeV and baryon chemical potential $\mu_B \lesssim 750$ MeV.

From a macroscopic view, the QCD phase transitions are characterized by the order parameters. More specifically, the chiral and the deconfinement phase transitions correspond to the chiral condensate $\langle\bar{q}q\rangle$ and the Polyakov loop Φ, respectively. Microscopically, the two order parameters are embedded in the Green's functions, i.e., the full quark propagator (inverse) in the language of functional approaches,

$$S_q^{-1}(p) = \mathrm{i}(\tilde{\omega}_n + gA_0)\gamma_4 Z_q^E(\boldsymbol{p},\tilde{\omega}_n) + \mathrm{i}\boldsymbol{\gamma}\cdot\boldsymbol{p} Z_q^M(\boldsymbol{p},\tilde{\omega}_n) + Z_q^E(\boldsymbol{p},\tilde{\omega}_n)M_q(\boldsymbol{p},\tilde{\omega}_n), \quad (2)$$

where $\tilde{\omega}_n = \omega_n + \mathrm{i}\mu_q$ with ω_n being the Matsubara frequencies, μ_q being the quark chemical potential, and $\boldsymbol{p}$ being the spatial momentum, along with Z_q^E, Z_q^M, and M_q being the dressing functions and A_0 being the gluon condensate. First, quite a number of studies have shown that the chiral condensate $\langle\bar{q}q\rangle$ is most dominantly related to the quark mass function M_q, and the validity of taking the M_q as the order parameter of chiral phase transition has been well known. Second, the gluon condensate A_0 is related to the Polyakov loop Φ as [47,48]

$$\Phi[A_0] = \frac{1}{N_c}\mathrm{tr}\mathcal{P}e^{\mathrm{i}\int_0^\beta dx_0 A_0}, \quad (3)$$

with $\beta = 1/T$, which is connected to the center symmetry breaking and thus the deconfinement. However, there are still ongoing quests for the functional approaches to connect the microscopic dynamics to the macroscopic thermodynamic observables, which involves explicitly an extraction of the QCD thermodynamic functions from the full momentum and Matsubara frequency dependent Green's functions; see, e.g., Refs. [49,50] for the recent progress.

In this work, we propose first a simplified framework of such a calculation with the approximation on the dressing functions at each (T,μ_q) in Eq. (2):

$$Z_q^{E,M}(\boldsymbol{p},\tilde{\omega}_n;T,\mu_q) \to 1,$$
$$M_q(\boldsymbol{p},\tilde{\omega}_n;T,\mu_q) \to M_q(0;T,\mu_q). \quad (4)$$

In particular, taking the quark mass function at zero momentum, i.e., the infrared limit, is a typical approximation to take care of the physics in the nonperturbative QCD regime; this leads then to a simplified expression for the quark propagator as:

$$S_q^{-1}(p) = \mathrm{i}[\tilde{\omega}_n + gA_0(T,\mu_q)]\gamma_4 + \mathrm{i}\boldsymbol{\gamma}\cdot\boldsymbol{p} + M_q(T,\mu_q); \quad (5)$$

in the expression, we have left out the momentum index in M_q and labeled the T and μ_q dependence in A_0 and M_q explicitly. Also, the expectation value of the gluon condensate A_0 can be converted into the Polyakov loop expectation value Φ since we will eventually apply the quark propagator to compute the number density. The general framework takes then two steps:

(i) The temperature and chemical potential dependence of the order parameters, namely, $M_q(T,\mu_q)$ (at zero momentum) and $\Phi(T,\mu_q)$, are taken from the functional QCD calculations [37,39,51], which incorporates the nonperturbative quantum, thermal, and density fluctuations. To note, the functional QCD method has also incorporated the full mesonic and baryonic effects, which is achieved in terms of dynamical quarks and gluons degrees of freedom.

For the convenience of further applications, a parametrized form of the order parameters is very helpful, which will be discussed in the remaining part of this section.

(ii) The obtained order parameters are installed into the quark propagator for a further calculation on the QCD EOS. We will see in the next section that the approximation equation (4) provides a simple analytical form available for the thermodynamic functions. Such a construction is the main purpose of this article, which has great advantages for further applications.

Now, for the quark mass function at zero momentum M_q, it is found that the functional QCD data [37,39] fit well with the feature of the three-dimensional (3D) Ising parametrization [52,53], by taking the CEP of chiral phase transition as the origin. We note that such a parametrization is phenomenologically motivated, considering that the CEP is recognized to be in the $Z(2)$ universality class. Moreover, the (preudo-)Goldstone modes become relevant near the CEP, which would also drive the CEP into the Ising universality class. Nevertheless, in principle, one can apply any reasonable parametrization numerically on the functional QCD data for the same purpose. The parametrized form of the quark mass function reads

$$M_q(T,\mu_q) = \frac{M_0}{2}[1 - \mathcal{M}_{\rm Ising}(T,\mu_B)]. \tag{6}$$

The typical mass scale for the light-flavor quarks $M_0 = 350$ MeV suggested by the lattice [54,55] and functional QCD [39,56] is naturally incorporated. The (T,μ_B) dependence in the QCD phase diagram is connected to the Ising parameters (r,h) as

$$\mathcal{M}_{\rm Ising} = \mathcal{M}_0 R^\beta \theta, \tag{7}$$

$$h = h_0 R^{\beta\delta} \tilde{h}(\theta), \tag{8}$$

$$r = R(1-\theta^2), \tag{9}$$

with the typical parameters $\beta = 0.326$, $\delta = 4.80$, $h_0 = 0.394$, and $\tilde{h}(\theta) = \theta(1 - 0.76201\theta^2 + 0.00804\theta^4)$ as given in Ref. [52] and where $\mathcal{M}_0$ is the normalization constant. The complete mapping procedure is $(T,\mu_B) \to (R,\theta) \to (r,h)$. To match the phase transition line Eq. (1) precisely, one can take a nonlinear mapping as

$$\begin{aligned} \frac{\mu_B - \mu_B^{\rm CEP}}{\mu_B^{\rm CEP}} &= -r\omega\rho\cos\alpha_1 - h\omega\cos\alpha_2, \\ \frac{T - T^{\rm CEP}}{T^{\rm CEP}} &= f_{\rm PT}(r) + h\omega\sin\alpha_2, \end{aligned} \tag{10}$$

with $\alpha_1 = \tan^{-1}(2\kappa\mu_B^{\rm CEP}/T_c(0)) = 7.0°$ and $\alpha_2 = \alpha_1 + 90°$ in our case. The mapping function $f_{\rm PT}$ is calibrated so that at $h = 0$ Eqs. (10) become exactly the parametric equations of the phase transition line in Eq. (1), which requires

$$f_{\rm PT}(r) = \frac{\mu_B^{\rm CEP}}{2T^{\rm CEP}}(2 - r\omega\rho\cos\alpha_1)r\omega\rho\sin\alpha_1. \tag{11}$$

Intuitively, the Ising parameter h is related to the "distance" toward the chiral phase transition temperature, and r is the projection coordinate on the chiral phase transition line. The fit parameters for the dynamical mass M_q are listed in Table I, together with the position of the CEP at $\mu_B = 600$ MeV which is taken from Ref. [37]. We note that such a CEP location corresponds to the quark chemical potentials $\mu_u = \mu_d = \mu_B/3$ and $\mu_s = 0$ in the functional QCD approaches. In the following sections, the CEP location is then fixed in the investigation of charge (Q) and strangeness (S) conditions with different chemical potential setups; i.e., the μ_Q and μ_S dependence of the CEP location is neglected. Such treatment on μ_Q is suitable due to the small isospin asymmetry in the heavy-ion collisions. As for μ_S, better knowledge is required about the strangeness effect on the light-flavor condensate via the gluon propagator and also via the hadron resonance channel, especially the hyperon and kaon channels, and the related study is planned in the future.

TABLE I. The mapping parameters of the light-flavor dynamical mass equations (6) to (10) to match the functional QCD results. The position of CEP is also attached for completeness.

ω	ρ	$\mathcal{M}_0$	$(T^{\rm CEP}, \mu_B^{\rm CEP})$ (MeV)
1.0	2.0	0.75	(118.1, 600)

For the Polyakov loop expectation value, we take the fRG result at zero chemical potential from Ref. [51], which is denoted as $\Phi(T,0) = L(t)$ with $t = T/T_c(0)$. The fit function is taken as

$$L(t) = 2\left[1 + \exp\left(\frac{1 + l_1 t^3}{m_1 t + m_2 t^6}\right)\right]^{-1}, \tag{12}$$

with $l_1 = 2.732$, $m_1 = 0.5495$, and $m_2 = 1.831$. For the Polyakov loop at finite chemical potential, we follow Ref. [47] to take the center average approximation on A_0 so that it involves the Cartan generator τ^3, with the eigenvalues $\phi = \{\pm\varphi/2, 0\}$:

$$A_0 = \frac{2\pi T}{g}\phi\tau^3, \qquad \Phi = \frac{1}{3}[1 + 2\cos(\pi\varphi)]. \tag{13}$$

Such an approximation is supported by the small deviation between the conjugated Polyakov loops Φ and $\Phi^\dagger$, typically for $\mu_B \lesssim 500$ MeV as shown in Ref. [39]. One advantage of the approximation is that the phase transition line can also be embedded in a straightforward way:

$$\Phi(T,\mu_q) = L(t_\Phi), \tag{14}$$

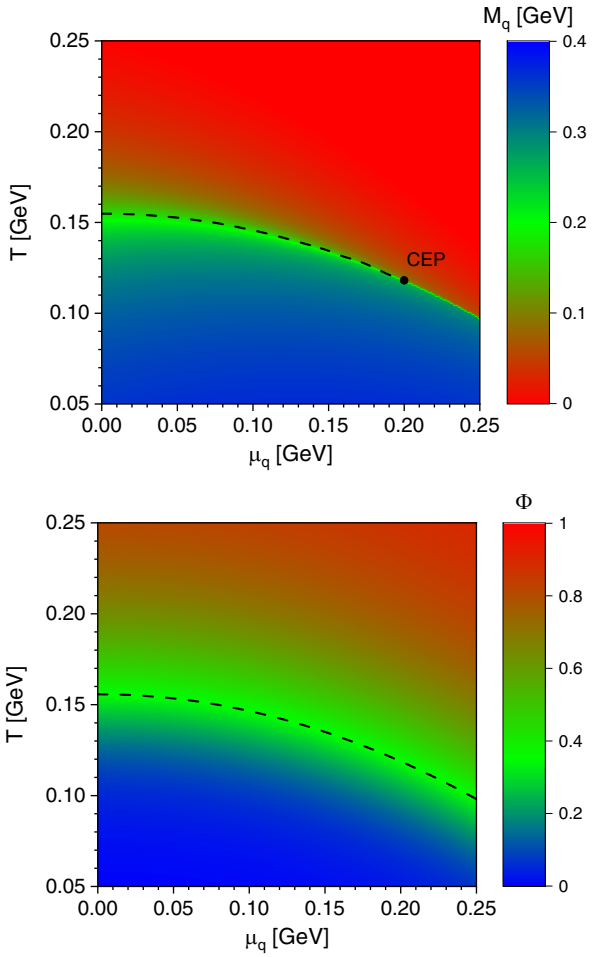

FIG. 1. The functional QCD based parametrization of the two order parameters M_q and Φ as functions of temperature T and chemical potential μ_q for light-flavor quarks. The two phase transition lines are shown as the black-dashed curve.

$$t_\Phi = \frac{T}{T_c(0)} + \kappa\left(\frac{3\mu_q}{T_c(0)}\right)^2. \tag{15}$$

By taking $T_c(0)$ and κ for the deconfinement phase transition the same as those for the chiral phase transition, which has been indicated by Refs. [33,39,57], the obtained Φ is consistent with the functional QCD data to a semi-quantitative level. In fact, such chemical-potential scaling behavior of the thermodynamic functions is also supported by other studies; see, e.g., Refs. [58–60].

To sum up, the parametrized form of the functional QCD based $M_q(T,\mu_q)$ and $\Phi(T,\mu_q)$ is obtained and is shown explicitly in Fig. 1. In addition, the phase transition lines, i.e., the (pseudo)critical temperature as a function of μ_B for the two phase transitions, are calculated and shown in Fig. 1 and are defined at the peak of the susceptibility,

$$\chi_\mathcal{O} = \frac{\partial\mathcal{O}}{\partial T}, \tag{16}$$

with $\mathcal{O} = -M_q$ for the chiral phase transition and $\mathcal{O} = \Phi$ for the deconfinement phase transition. The current results are consistent with the phase transition line obtained by lattice QCD simulations at small chemical potential [28–30] and functional QCD methods [37–39] with a CEP at $(T,\mu_B) = (118, 600)$ MeV [37–39,45]. Note that the chiral and deconfinement phase transition lines are not necessarily identical, which may induce some new phases like the quarkyonic phase [57,61–63]. Since the QCD phase transition is mainly characterized by the chiral phase transition, deviation of the two phase transitions may only induce some delicate changes in the observables, which require further investigations in the future.

III. CONSTRUCTION OF THE EOS IN A FUNCTIONAL QCD-BASED SCHEME

Lattice QCD simulations have delivered solid computations on the QCD EOS at vanishing chemical potential [64–66]. However, because of the sign problem, it is difficult for lattice QCD to reach real chemical potentials directly. The Taylor expansion approach [67–70] or alternative expansion scheme [58,71–73] is also limited in the small chemical potential region, and the latest lattice QCD results can only cover up to $\mu_B/T \leq 3.5$. On the other hand, the large chemical potential region is accessible by the functional QCD approaches, especially for the order parameters discussed in the last section. Therefore, one may combine the advantages of the two methods.

In this work, this is done by calculating the finite chemical potential effect through the integral relation between the QCD pressure P and the quark number densities $\{n_q\}$ [74–76],

$$P(T,\boldsymbol{\mu}) = P(T,\mathbf{0}) + \sum_q \int_0^{\mu_q} n_q(T,\mu)\mathrm{d}\mu, \tag{17}$$

with the assistance of lattice QCD EOS data at zero chemical potential $P(T,\mathbf{0})$, which has now been well determined from the lattice QCD simulations through the form of the trace anomaly $I(T)$ [65],

$$P(T,\mathbf{0})/T^4 = \int_0^T \mathrm{d}T'(I(T')/T'), \tag{18}$$

$$I(T) = e^{-h_1/t - h2/t^2}\cdot\left[h_0 + f_0\cdot\frac{\tanh(f_1 t + f_2) + 1}{1 + g_1 t + g_2 t^2}\right], \tag{19}$$

with $t = T/(200\ \mathrm{MeV})$, $h_0 = 0.1396$, $h_1 = -0.1800$, $h_2 = 0.0350$, $f_0 = 2.76$, $f_1 = 6.79$, $f_2 = -5.29$, $g_1 = -0.47$, and $g_2 = 1.04$ for $2+1$ flavor. Therefore, the key quantity for the EOS at finite chemical potential is the quark number density. In general, it is related to the full

momentum dependent quark propagator S_q in Eq. (2) as

$$n_q = -T\sum_n \int \frac{\mathrm{d}^3\boldsymbol{p}}{(2\pi)^3}\mathrm{tr}_{C,D}[\gamma_4 S_q(\boldsymbol{p},\omega_n)], \tag{20}$$

with the trace taken over the color index and the Dirac structure. Now, with the approximation equations (4) and (5), a simple analytical form is available for the number density. Specifically, the quark number density n_q in the (T,μ_q) plane can be expressed by the two order parameters M_q and Φ as follows:

$$n_q(T,\mu_q) = 2N_c \int \frac{\mathrm{d}^3\boldsymbol{k}}{(2\pi)^3}[f_q^+(\boldsymbol{k};T,\mu_q) - f_q^-(\boldsymbol{k};T,\mu_q)], \tag{21}$$

$$f_q^{\pm} = \frac{\Phi(T,\mu_q)x_\pm^2 + 2\Phi(T,\mu_q)x_\pm + 1}{x_\pm^3 + 3\Phi(T,\mu_q)x_\pm^2 + 3\Phi(T,\mu_q)x_\pm + 1}, \tag{22}$$

$$x_\pm(\boldsymbol{k};T,\mu_q) = \exp\left[(E_q(\boldsymbol{k};T,\mu_q) \mp \mu_q)/T\right], \tag{23}$$

$$E_q(\boldsymbol{k};T,\mu_q) = \sqrt{\boldsymbol{k}^2 + M_q^2(T,\mu_q)}. \tag{24}$$

Taking the results of $M_q(T,\mu_q)$ and $\Phi(T,\mu_q)$ from Sec. II, this then completes our functional QCD based framework for the EOS, which incorporates the up-to-date knowledge of the QCD phase structure through the order parameters. As we will demonstrate in the following, the obtained EOS is comparable with the lattice QCD prediction and the experimental observations quantitatively at small chemical potential, which opens an access of quantitative estimations on the QCD thermodynamic properties toward the chemical potential region of the possible CEP and the first-order phase transitions.

IV. NUMERICAL RESULTS OF THE EOS WITH FIRST-ORDER PHASE TRANSITION

We proceed with an investigation on the $(2+1)$-flavor QCD EOS, which involves the baryon, electric charge, and strangeness chemical potentials (μ_B,μ_Q,μ_S). These chemical potentials are associated with the quark chemical potentials as

$$\mu_u = \frac{1}{3}\mu_B + \frac{2}{3}\mu_Q, \tag{25}$$

$$\mu_d = \frac{1}{3}\mu_B - \frac{1}{3}\mu_Q, \tag{26}$$

$$\mu_s = \frac{1}{3}\mu_B - \frac{1}{3}\mu_Q - \mu_S. \tag{27}$$

To be consistent with the hydrodynamic simulations, we first consider the three-flavor degenerate case (case B)

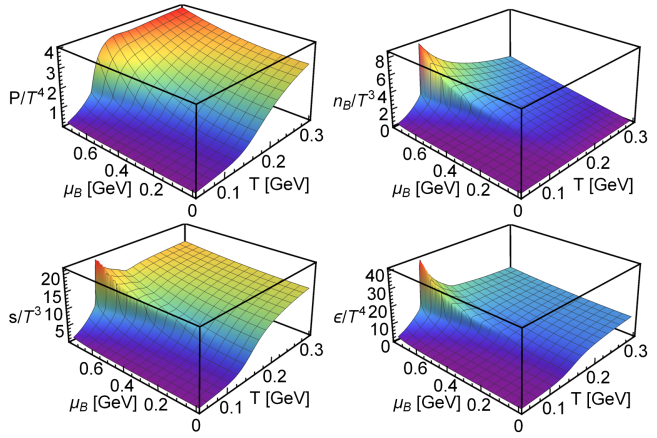

FIG. 2. Calculated 3D plots for the pressure, number density, entropy density, and energy density in terms of the temperature and chemical potential, normalized to a dimensionless form by the temperature T with the respective power.

with $\mu_u = \mu_d = \mu_s = \frac{\mu_B}{3}$, which is the conventional case often applied in the hydrodynamics simulations. With the obtained pressure $P(T,\mu_B)$ and number density $n_q(T,\mu_B)$ and using thermodynamic relations, one can compute the entropy density $s = \partial P/\partial T$, the energy density $\varepsilon = Ts - P + \mu_B n_B$, and so on. We show thus the 3D plot in terms of temperature and chemical potential for the pressure, baryon number density, entropy density, and energy density in Fig. 2. The isentropic speed of sound squared c_s^2 is also calculated by

$$c_s^2 = \left(\frac{\partial p}{\partial \varepsilon}\right)_{s/n_B} = \frac{n_B^2\partial_T^2 P - 2sn_B\partial_T\partial_{\mu_B}P + s^2\partial_{\mu_B}^2 P}{(\varepsilon+P)[\partial_T^2 P\partial_{\mu_B}^2 P - (\partial_T\partial_{\mu_B}P)^2]}, \tag{28}$$

and the result is given in Fig. 3.

Now, one may take a closer look at the EOS [strictly speaking, its slope defined with Eq. (28)] at different chemical potentials as depicted in Fig. 3. For small chemical

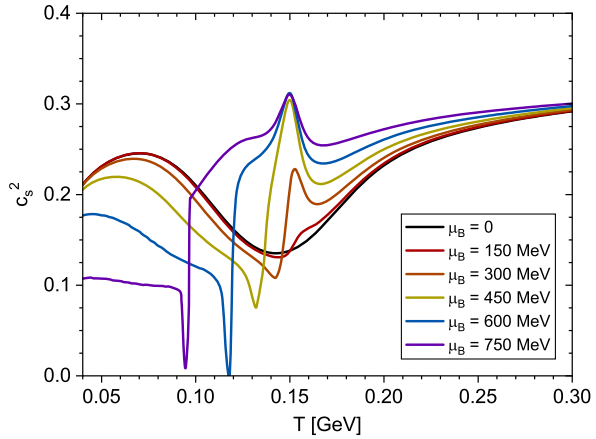

FIG. 3. Calculated speed of sound squared as a function of temperature T at several values of the baryon chemical potential μ_B.

potentials, the speed of sound is a smooth function with a minimum around $c_s^2 \sim 0.12$ at phase transition point. As the chemical potential becomes larger, the speed of sound becomes more oscillated near the transition temperature. At the CEP and the first-order phase transition region, the speed of sound at the phase transition point becomes zero. For the first-order phase transition, since one has $dP = 0$ and a finite $d\varepsilon$ during the phase transition, the curve becomes discontinuous for the two phases. The speed of sound in the vicinity of the phase transition point is still finite, and only a few points reach zero drastically. More interestingly, as the chemical potential increases, there appears a peak nearly above the phase transition temperature. The maximum value of the peak gradually grows and saturates to the conformal limit $c_s^2 = 1/3$, which implies a new feature of the QCD EOS at high densities.

In the ideal case of the first-order phase transition, there exists discontinuity in the number density, entropy density, and also energy density. The discontinuity would be affected by the nonequilibrium effects in the dynamical evolution and will cause problems in the hydrodynamics simulation. Here, we consider the Maxwell construction to fill the discontinuity with simply a linear transition of the thermodynamic functions from one phase to the other. This construction leads to a vanishing speed of sound during the first-order phase transition. To consider the spinodal decomposition, one may need a construction described in Ref. [52], and the speed of sound will be negative in the instable region. In Fig. 4, we show the construction for the pressure as the function of energy density. Using this construction, one can convert the thermodynamic quantities from the (T, μ_B) dependence into the (ε, n_B) dependence, which is then accessible for the hydrodynamic simulations.

At last, we check the conserved charge conditions satisfied in the heavy-ion collisions. Considering the three light flavors $f = u, d, s$, the conditions are

$$n_S = 0, \qquad n_Q/n_B = r, \tag{29}$$

with conserved charges $n_{B,Q,S}$ which stand for the baryon, electric, and strangeness densities, respectively, and where r is the charge-to-mass ratio of the collided nuclei, e.g., $r_{\mathrm{Au+Au}} \approx 0.4$.

In this sense the three-flavor-degenerate scenario is equivalent to $\mu_Q = \mu_S = 0$ in Eqs. (25) to (27); i.e., only the baryon chemical potential is considered. On the other hand, for the $(2+1)$-flavor scenario, Eq. (29) is equivalent to

$$n_s = -n_S = 0, \tag{30}$$

$$\frac{2n_u(T,\mu_u) - n_d(T,\mu_d)}{n_u(T,\mu_u) + n_d(T,\mu_d)} = r. \tag{31}$$

Therefore, for the charge conserved case, the remaining task is to consistently solve Eqs. (25), (26), and (31).

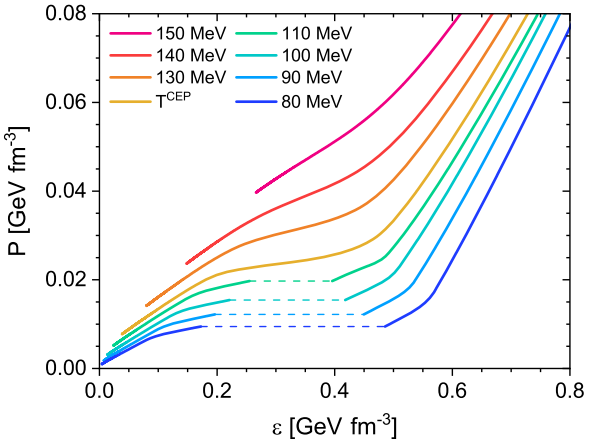

FIG. 4. Obtained pressure as a function of the energy density at several given temperatures; the Maxwell construction is displayed as the dashed lines.

The parameters in Table I are implemented for both u and d quark densities in Eq. (31).

We show the calculated isentropic trajectories with $s/n_B = \mathrm{const}$ in Fig. 5, for the three-flavor-degenerate case, which is denoted as B (baryon), and the charge-conserved case with the constraint of the conserved charge conditions, which is denoted as BS (baryon strange). The obtained isentropic trajectories are in good agreement with the lattice QCD result [70]. It shows that the strangeness neutrality pushes the trajectories into the higher chemical potential region, which may have an impact on the initial conditions of heavy-ion collisions [77–80].

Moreover, we investigate the baryon number fluctuations, i.e., the μ_B susceptibilities:

$$\chi_k^B = \frac{\partial^k (P/T^4)}{\partial(\mu_B/T)^k}, \quad k = 1, 2, \ldots. \tag{32}$$

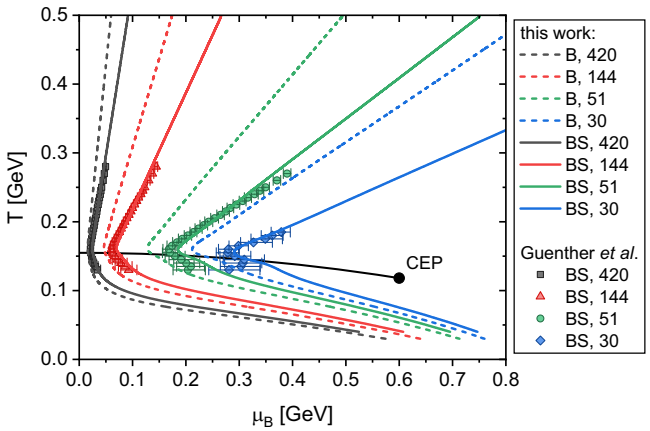

FIG. 5. Calculated isentropic trajectories at $s/n_B = 420, 144, 51,$ and 30, with the three-flavor-degenerate EOS (B) and the charge-conserved EOS (BS). The scatter points are the trajectories obtained from lattice QCD calculation [70] at these s/n_B values.

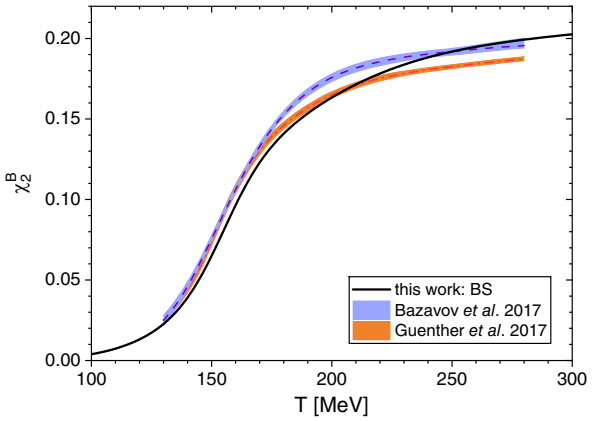

FIG. 6. Calculated baryon number susceptibility χ_2^B at $\mu_B = 0$, compared with the lattice results extracted from the Taylor expansion [69,70].

Reference [81] shows within an up-to-date functional QCD framework that the high-order susceptibilities can be well compared to the lattice QCD results. Therefore, a quantitative check of the susceptibilities is helpful for the validity of the present simplification in Eqs. (4). First, we compare our result of the leading susceptibility χ_2^B at vanishing μ_B, in the BS case, for example, which is in good agreement with the corresponding lattice QCD results obtained from the Taylor expansion scheme (continuum limit) [69,70] in Fig. 6. Second, we further checked higher-order susceptibilities such as χ_4^B with lattice QCD results, and the comparison is less satisfied than the χ_2^B, with an overall deviation of about 20% for different temperatures. This implies then the limitation about the simplification equations (4), as it is better suited to describe the lower-order thermodynamic functions,

$$\partial_T^i \partial_{\mu_B}^j P \quad \text{for } i + j \lesssim 2, \tag{33}$$

and for not very high μ_B. Fortunately, the comparison given in Fig. 5 already shows that the framework is suitable at least up to $\mu_B = 400$ MeV, which corresponds to an intermediate collision energy. Also, the speed of sound squared Eq. (28) satisfies the condition of Eq. (33), which is the key ingredient for the application on hydrodynamical simulations.

In addition, one may also consider the cross-correlators such as χ^{BQ} and χ^{BS}, which reflect the properties of conserved charges: the baryon charge (B), electric charge (Q), and strangeness (S). This corresponds explicitly to the coupling between the baryon number to the electric charge and/or strangeness numbers, which involves an evaluation on the chemical potential derivatives, e.g., $\frac{\partial \mu_Q}{\partial \mu_B}$ and $\frac{\partial \mu_S}{\partial \mu_B}$. However, as discussed in Sec. II, this has not yet been implemented systematically in our work, which essentially requires knowledge on the μ_S and μ_Q effects on the light-flavor quark condensate, and moreover, on the Polyakov loop. Hence, the cross-correlators require further improvements beyond the present framework.

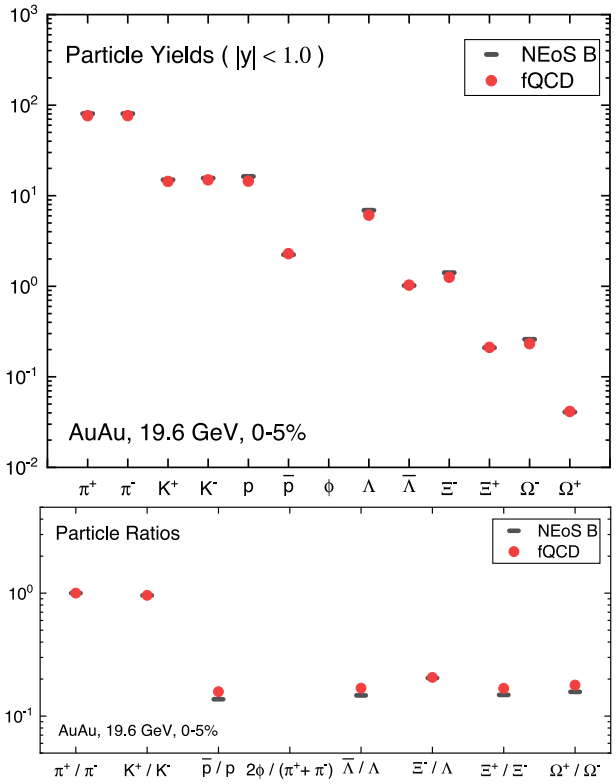

FIG. 7. Identified thermal particle yields (upper panel) and their ratios (lower panel) in 0%–5% Au + Au collisions at $\sqrt{s_{NN}} = 19.6$ GeV. The scatters represent the model calculations NEOS-B (lattice QCD + hadron resonance gas model, see Ref. [85]) and fQCD equations of state on the freeze-out surface, respectively.

To evaluate the applicability of the constructed fQCD EOS in realistic dynamical evolution, we implement the relativistic viscous hydrodynamic model MUSIC [82,83] to calculate the observables of thermal particles without hadronic scattering or decay effects. See Ref. [84] for more details of the model. Figure 7 shows the identified particle yields and their ratios in 0%–5% Au + Au collisions at $\sqrt{s_{NN}} = 19.6$ GeV. It is apparent that the present fQCD results are consistent with those from the NEOS-B, which is an EOS based on a combination of the lattice QCD simulation result at high and intermediate temperatures and the hadron resonance gas model result at low temperature [85]. These particle yields together with other checks, for instance, about the elliptic flow and p_T spectra, show evidently that, in the crossover region, changing the EOS will not make an obvious difference to the bulk evolution. In addition, this fQCD EOS also works stably at the high baryon number density region, including the case of a first-order phase transition, which is useful in future studies when combined with the bulk viscosity and other non-equilibrium effects.

To close this section, we note that the EOS data as a function of T and μ_B together with the MUSIC input format for both B and BS cases are available on GitHub (fQCD-EoS-PhaseDiagramMap) [86].

V. CONCLUSIONS

We proposed a construction on the QCD EOS in a functional QCD based scheme, which utilizes the knowledge of the QCD phase diagram and the order parameters at finite density from functional QCD approaches, i.e. the phase transition line and the location of the CEP. By implementing the zero-momentum approximation, the quark number density is expressed analytically, which ensures then that the EOS can be analytically calculated and is convenient for further applications.

We computed the thermodynamic quantities such as the pressure, the energy density and the entropy density, and eventually the speed of sound as a function of temperature and chemical potential. For small chemical potentials, the obtained minimum around $c_s^2 \sim 0.12$ at the phase transition point is consistent with the results of lattice QCD simulation. As the chemical potential increases, the speed of sound drops drastically to zero at the phase transition point. Moreover, the speed of sound at large chemical potential shows a conformal limit behavior right after the first-order phase transition, which implies a new feature of the QCD EOS at high density.

We also combine the EOS with the hydrodynamic simulation. For Au + Au collisions at $\sqrt{s_{NN}} = 19.6$ GeV, our results on the particle yields and ratios are in good agreement with the results from the commonly used NEOS. Moreover, we have tested that with the current EOS it is possible for the hydrodynamic simulations to reach the first-order phase transition region. A more realistic dynamical description of the first-order phase transition will be investigated in the future.

ACKNOWLEDGMENTS

F. G. and Y. L. thank the other members of the fQCD Collaboration [87] for discussions and collaboration on related subjects. This work is supported by the National Natural Science Foundation of China under Grants No. 12247107, No. 12175007, and No. 12075007. B. C. F. is also supported by the National Natural Science Foundation of China under Grant No. 12147173. F. G. is supported by the National Science Foundation of China under Grant No. 12305134.

[1] Y. Akiba *et al.*, arXiv:1502.02730.
[2] X. Luo and N. Xu, Nucl. Sci. Tech. **28**, 112 (2017).
[3] J. Adamczewski-Musch *et al.* (HADES Collaboration), Nat. Phys. **15**, 1040 (2019).
[4] A. Lovato *et al.*, arXiv:2211.02224.
[5] N. Alizadehvandchali *et al.* (ALICE-USA Collaboration), arXiv:2212.00512.
[6] M. Arslandok *et al.*, arXiv:2303.17254.
[7] H.-T. Ding, Proc. Sci. LATTICE2016 (2017) 022.
[8] J. N. Guenther, Eur. Phys. J. A **57**, 136 (2021).
[9] A. Monnai, B. Schenke, and C. Shen, Int. J. Mod. Phys. A **36**, 2130007 (2021).
[10] O. Philipsen, Symmetry **13**, 2079 (2021).
[11] F. Karsch, arXiv:2212.03015.
[12] C. Ratti, Prog. Part. Nucl. Phys. **129**, 104007 (2023).
[13] A. Sorensen *et al.*, Prog. Part. Nucl. Phys. **134**, 104080 (2024).
[14] M. Buballa, Phys. Rep. **407**, 205 (2005).
[15] K. Fukushima and C. Sasaki, Prog. Part. Nucl. Phys. **72**, 99 (2013).
[16] B.-J. Schaefer, J. M. Pawlowski, and J. Wambach, Phys. Rev. D **76**, 074023 (2007).
[17] B.-J. Schaefer and M. Wagner, Prog. Part. Nucl. Phys. **62**, 381 (2009).
[18] W. J. Fu, Z. Zhang, and Y. X. Liu, Phys. Rev. D **77**, 014006 (2008).
[19] G. Y. Shao, M. Di Toro, V. Greco, M. Colonna, S. Plumari, B. Liu, and Y. X. Liu, Phys. Rev. D **84**, 034028 (2011).
[20] X. Y. Xin, S. X. Qin, and Y. X. Liu, Phys. Rev. D **90**, 076006 (2014).
[21] S. He, S.-Y. Wu, Y. Yang, and P.-H. Yuan, J. High Energy Phys. 04 (2013) 093.
[22] K. Chelabi, Z. Fang, M. Huang, D. Li, and Y.-L. Wu, J. High Energy Phys. 04 (2016) 036.
[23] T. Kojo, D. Hou, J. Okafor, and H. Togashi, Phys. Rev. D **104**, 063036 (2021).
[24] X. Chen, L. Zhang, D. Li, D. Hou, and M. Huang, J. High Energy Phys. 07 (2021) 132.
[25] M. Hippert, J. Grefa, T. A. Manning, J. Noronha, J. Noronha-Hostler, I. Portillo Vazquez, C. Ratti, R. Rougemont, and M. Trujillo, arXiv:2309.00579.
[26] R. G. Cai, S. He, L. Li, and Y. X. Wang, Phys. Rev. D **106**, L121902 (2022).
[27] X. Chen, D. Li, and M. Huang, Chin. Phys. C **43**, 023105 (2019).
[28] S. Borsanyi, Z. Fodor, J. N. Guenther, R. Kara, S. D. Katz, P. Parotto, A. Pasztor, C. Ratti, and K. K. Szabo, Phys. Rev. Lett. **125**, 052001 (2020).

[29] A. Bazavov *et al.* (HotQCD Collaboration), Phys. Lett. B **795**, 15 (2019).
[30] C. Bonati, M. D'Elia, F. Negro, F. Sanfilippo, and K. Zambello, Phys. Rev. D **98**, 054510 (2018).
[31] C. D. Roberts and S. M. Schmidt, Prog. Part. Nucl. Phys. **45**, S1 (2000).
[32] S. X. Qin, L. Chang, H. Chen, Y. X. Liu, and C. D. Roberts, Phys. Rev. Lett. **106**, 172301 (2011).
[33] C. S. Fischer, J. Luecker, and C. A. Welzbacher, Phys. Rev. D **90**, 034022 (2014).
[34] F. Gao and Y. X. Liu, Phys. Rev. D **94**, 076009 (2016).
[35] C. S. Fischer, Prog. Part. Nucl. Phys. **105**, 1 (2019).
[36] F. Gao and J. M. Pawlowski, Phys. Rev. D **102**, 034027 (2020).
[37] F. Gao and J. M. Pawlowski, Phys. Lett. B **820**, 136584 (2021).
[38] P. J. Gunkel and C. S. Fischer, Phys. Rev. D **104**, 054022 (2021).
[39] W. J. Fu, J. M. Pawlowski, and F. Rennecke, Phys. Rev. D **101**, 054032 (2020).
[40] N. Dupuis, L. Canet, A. Eichhorn, W. Metzner, J. M. Pawlowski, M. Tissier, and N. Wschebor, Phys. Rep. **910**, 1 (2021).
[41] W. J. Fu, Commun. Theor. Phys. **74**, 097304 (2022).
[42] D. Binosi and J. Papavassiliou, Phys. Rep. **479**, 1 (2009).
[43] G. Eichmann, H. Sanchis-Alepuz, R. Williams, R. Alkofer, and C. S. Fischer, Prog. Part. Nucl. Phys. **91**, 1 (2016).
[44] J. M. Pawlowski, Ann. Phys. (Amsterdam) **322**, 2831 (2007).
[45] W. J. Fu, X. Luo, J. M. Pawlowski, F. Rennecke, and S. Yin, arXiv:2308.15508.
[46] G. Eichmann, C. S. Fischer, and C. A. Welzbacher, Phys. Rev. D **93**, 034013 (2016).
[47] C. S. Fischer, L. Fister, J. Luecker, and J. M. Pawlowski, Phys. Lett. B **732**, 273 (2014).
[48] L. Fister and J. M. Pawlowski, Phys. Rev. D **88**, 045010 (2013).
[49] W. J. Fu, J. M. Pawlowski, and F. Rennecke, SciPost Phys. Core **2**, 002 (2020).
[50] Y. Lu, F. Gao, Y. X. Liu, and J. M. Pawlowski, arXiv: 2310.18383.
[51] W. J. Fu and J. M. Pawlowski, Phys. Rev. D **92**, 116006 (2015).
[52] P. Parotto, M. Bluhm, D. Mroczek, M. Nahrgang, J. Noronha-Hostler, K. Rajagopal, C. Ratti, T. Schäfer, and M. Stephanov, Phys. Rev. C **101**, 034901 (2020).
[53] T. Dore, J. M. Karthein, I. Long, D. Mroczek, J. Noronha-Hostler, P. Parotto, C. Ratti, and Y. Yamauchi, Phys. Rev. D **106**, 094024 (2022).
[54] P. O. Bowman, U. M. Heller, D. B. Leinweber, M. B. Parappilly, A. G. Williams, and J.-b. Zhang, Phys. Rev. D **71**, 054507 (2005).
[55] O. Oliveira, A. Kızılersu, P. J. Silva, J.-I. Skullerud, A. Sternbeck, and A. G. Williams, Acta Phys. Pol. B Proc. Suppl. **9**, 363 (2016).
[56] F. Gao, J. Papavassiliou, and J. M. Pawlowski, Phys. Rev. D **103**, 094013 (2021).
[57] L. F. Chen, S. X. Qin, and Y. X. Liu, Phys. Rev. D **102**, 054015 (2020).
[58] S. Borsányi, Z. Fodor, J. N. Guenther, R. Kara, S. D. Katz, P. Parotto, A. Pásztor, C. Ratti, and K. K. Szabó, Phys. Rev. Lett. **126**, 232001 (2021).
[59] S. Mondal, S. Mukherjee, and P. Hegde, Phys. Rev. Lett. **128**, 022001 (2022).
[60] S. Mukherjee, F. Rennecke, and V. V. Skokov, Phys. Rev. D **105**, 014026 (2022).
[61] F. Gao and Y. X. Liu, Phys. Rev. D **94**, 094030 (2016).
[62] O. Philipsen and J. Scheunert, J. High Energy Phys. 11 (2019) 022.
[63] O. Philipsen, P. Lowdon, L. Y. Glozman, and R. D. Pisarski, Proc. Sci. LATTICE2022 (**2023**) 189.
[64] F. Karsch, Nucl. Phys. **A698**, 199 (2002).
[65] S. Borsanyi, G. Endrodi, Z. Fodor, A. Jakovac, S. D. Katz, S. Krieg, C. Ratti, and K. K. Szabo, J. High Energy Phys. 11 (2010) 077.
[66] A. Bazavov *et al.* (HotQCD Collaboration), Phys. Rev. D **90**, 094503 (2014).
[67] A. Bazavov *et al.*, Phys. Rev. D **101**, 074502 (2020).
[68] S. Borsanyi, Z. Fodor, J. N. Guenther, S. K. Katz, K. K. Szabo, A. Pasztor, I. Portillo, and C. Ratti, J. High Energy Phys. 10 (2018) 205.
[69] A. Bazavov *et al.*, Phys. Rev. D **95**, 054504 (2017).
[70] J. N. Guenther, R. Bellwied, S. Borsanyi, Z. Fodor, S. D. Katz, A. Pasztor, C. Ratti, and K. K. Szabó, Nucl. Phys. **A967**, 720 (2017).
[71] P. Parotto, S. Borsányi, Z. Fodor, J. N. Guenther, R. Kara, A. Pásztor, C. Ratti, and K. K. Szabó, EPJ Web Conf. **276**, 01014 (2023).
[72] D. Bollweg, D. A. Clarke, J. Goswami, O. Kaczmarek, F. Karsch, S. Mukherjee, P. Petreczky, C. Schmidt, and S. Sharma (HotQCD Collaboration), Phys. Rev. D **108**, 014510 (2023).
[73] D. Bollweg, J. Goswami, O. Kaczmarek, F. Karsch, S. Mukherjee, P. Petreczky, C. Schmidt, and P. Scior (HotQCD Collaboration), Phys. Rev. D **105**, 074511 (2022).
[74] H. Chen, M. Baldo, G. F. Burgio, and H. J. Schulze, Phys. Rev. D **86**, 045006 (2012).
[75] P. Isserstedt, C. S. Fischer, and T. Steinert, Phys. Rev. D **103**, 054012 (2021).
[76] F. Gao and I. M. Oldengott, Phys. Rev. Lett. **128**, 131301 (2022).
[77] W. J. Fu, J. M. Pawlowski, and F. Rennecke, Phys. Rev. D **100**, 111501 (2019).
[78] J. Noronha-Hostler, P. Parotto, C. Ratti, and J. M. Stafford, Phys. Rev. C **100**, 064910 (2019).
[79] L. Jiang and J. Chao, Eur. Phys. J. A **59**, 30 (2023).
[80] K.-J. Sun, W.-H. Zhou, L.-W. Chen, C. M. Ko, F. Li, R. Wang, and J. Xu, arXiv:2205.11010.
[81] W.-j. Fu, X. Luo, J. M. Pawlowski, F. Rennecke, R. Wen, and S. Yin, Phys. Rev. D **104**, 094047 (2021).
[82] B. Schenke, S. Jeon, and C. Gale, Phys. Rev. C **82**, 014903 (2010).
[83] B. Schenke, S. Jeon, and C. Gale, Phys. Rev. C **85**, 024901 (2012).

[84] B. Fu, K. Xu, X.-G. Huang, and H. Song, Phys. Rev. C **103**, 024903 (2021).
[85] A. Monnai, B. Schenke, and C. Shen, Phys. Rev. C **100**, 024907 (2019).
[86] https://github.com/YiLu1048576/fQCD-EoS-PhaseDiagramMap.git.
[87] J. Braun, Y.-R. Chen, W. J. Fu, F. Gao, A. Geissel, J. Horak, C. Huang, F. Ihssen, Y. Lu, J. M. Pawlowski, F. Rennecke, F. Sattler, B. Schallmo, J. Stoll, Y.-Y. Tan, S. Töpfel, J. Turnwald, R. Wen, J. Wessely, N. Wink, S. Yin, and N. Zorbach (2023).